Towards using Thermal Cameras in Birth Detection

Jorge García-Torres*, Øyvind Meinich-Bache*, Sara Brunner†, Anders Johannessen†,
Siren Rettedal‡§ and Kjersti Engan*
*Dept. Electrical Engineering and Computer Science, University of Stavanger, Norway
Email: {jorge.garcia-torres, oyvind.meinich-bache, kjersti.engan}@uis.no
†Laerdal Medical AS, Stavanger, Norway
‡Dept. of Paediatrics, Stavanger University Hospital, Norway
§Faculty of Health Sciences, University of Stavanger, Norway

***Abstract*—In recent years, thermal imaging has been used in numerous applications due to its ability to capture and visualize the thermal radiation emitted by objects. Thermal cameras can be employed as non-invasive systems for detecting variations in temperatures while protecting privacy in case people are involved. Due to this, thermal imaging is especially suitable in surveillance and medical applications. However, the accuracy of commercial uncooled thermal cameras is usually too low to provide the user with a precise temperature value of a target object under real-world conditions. This paper aims to investigate the challenges of performing accurate temperature measurements when using thermal imaging during birth scenarios. Our results demonstrate that temperature estimates are susceptible to several factors when measuring in delivery room environments.**

Keywords*—Thermal imaging, thermal cameras, time of birth detection.

I. Introduction

Thermal imaging has become a very appealing technology for applications where visualizing temperature variations is required. By capturing the amount of thermal radiation of all objects in a scene, thermal cameras are able to estimate their temperature. Thermal imaging was initially used for military applications and surveillance. Through the development of low-cost thermal detectors using uncooled infrared microbolometer arrays [1], [2], this technology has become more accessible and applicable for other scenarios, e.g., analysis of volcanic activity [3], non-destructive testing [4], [5], industrial safety [6], precision agriculture [7], people detection [8], ambient assistant living systems [9], and self-driving vehicles [10]. In the medical field, thermal imaging has initially been used for non-invasive monitoring of human skin temperature [11]. Later on, several medical applications have used this technology for, among others: breast cancer detection [12], skin cancer detection [13], stress detection [14], and diagnosis of fever, hypothermia, diabetes and vascular disorders [15]. Recently, triggered by the emergence of COVID-19, the use of thermal imaging to detect people with elevated body temperature has increased, as described in [16]–[18].

However, as most of the mentioned papers reported, it is difficult to get an accurate temperature measurement of a particular object by using a thermal camera. Not only can multiple sources of thermal energy be found in the scene, but also several factors may distort the measurement. Various studies have analyzed the relevance of the distance [19], size-of-source effect [20], camera field of view [21], and angle of view [21], [22] when measuring temperature. Furthermore, thermal sensor fabrication is very complex, resulting in devices of uneven quality. More accurate thermal cameras are available at a much higher price or restricted to military purposes.

This paper aims to provide the reader with a better understanding of the existing challenges of using an uncooled thermal camera to measure temperature values in real-world environments accurately. As illustrated in Fig. 1, the birth scenario with a dual thermal sensor setup is used as an example for this study. Four experiments were carried out to analyze fluctuations in the temperature measurements and the challenges of using thermal cameras. This study is the preliminary step for developing a time of birth detector based on artificial intelligence (AI) and thermal imaging. Currently, there exists no automated solution for the time of birth detection. It is recorded manually in minute precision and can be potentially unreliable. The skin temperature of the newborn immediately after birth is approximately 37°C, which is higher than the skin temperature of other people in the room. Thus, thermal imaging can be used for detecting the exact time of birth while respecting privacy of the healthcare personnel and the mothers. Videos recorded with thermal cameras from natural births and simulations at the Stavanger University Hospital (SUS) were utilized for the experiments. This research is part of the NewbornTime[1] project, which aims to improve newborn care by using AI for activity and event recognition in video during and after birth.

II. Thermal Radiation

Thermal radiation is the electromagnetic radiation emitted by any object with a temperature above absolute zero. At temperatures relatively close to ambient temperature, thermal radiation is typically concentrated around the mid- and long-wavelength infrared bands (3 to 15 μm) [23] and many thermal cameras are designed to capture radiation within this wavelength. The thermal radiation E emitted per unit area by an object with perfect emission properties (black body) is dependent on its temperature T in accordance with the Stefan-Boltzmann formula [24]:

$$E = \varphi T^4 \tag{1}$$

[1]https://www.uis.no/newborntime

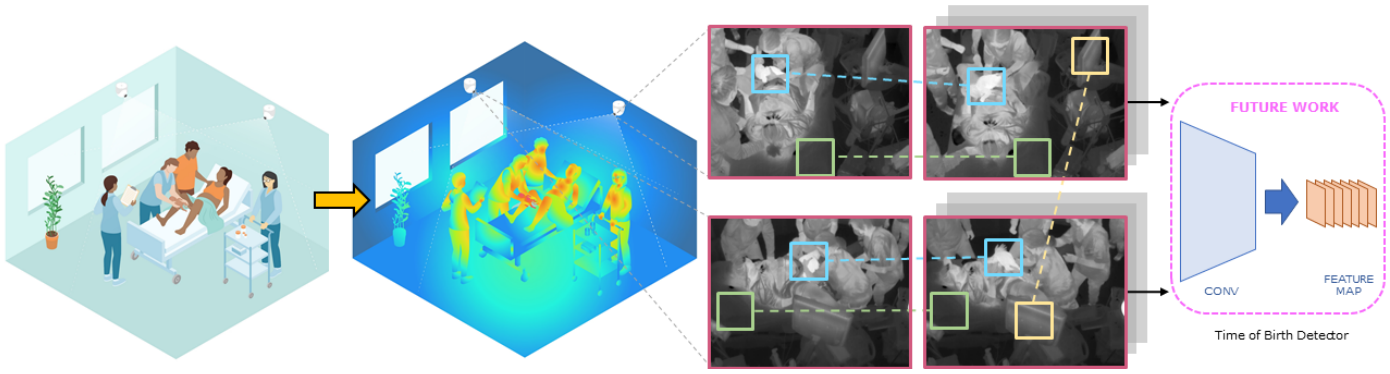

Fig. 1. Representation of a delivery room at SUS. As illustrated, the use of thermal imaging ensures the privacy of patients and healthcare personnel. Thermal radiation captured by the sensors is provided as intensity values (single-channel values). Video frames can therefore be represented as grayscale images. Four situations causing fluctuations are analyzed in our experiments: Exp. 1 in green, noise variation over time in a fixed region of interest; Exp. 2 in blue, changes in the target object's position relative to the sensor module; Exp. 3 in yellow, disparity between the estimated temperature values provided by two different sensors on the same region of interest; and Exp. 4 in red, effect of room temperature in measurements.

where $\varphi \approx 5.67 \times 10^{-8} W \cdot m^{-2} \cdot K^{-4}$ is the Stefan–Boltzmann constant.

For any real object, absorptivity α is the ability to absorb thermal radiation; emissivity ϵ refers to the ability to emit thermal radiation; reflectance ρ is the ability to reflect the radiation incident on its surface; and transmittance τ is the ability to transmit radiation through it. The sum of the absorptivity, reflectance and transmittance is equal to 1 ($\alpha + \rho + \tau = 1$). For opaque objects in thermodynamic equilibrium, there is no transmitted radiation ($\tau = 0$), and the emitted and absorbed thermal radiation are equal ($\epsilon = \alpha$) according to the Kirchhoff's law of thermal radiation [25]. The emissivity of real objects is experimentally estimated and expressed in a range from 0 (perfect mirror) to 1 (ideal black body). For human skin, emissivity is considered to be 0.98 ± 0.01 [26]. In practice, the total incident radiation E_{tot} captured by a thermal camera can be expressed as the sum of the emitted radiation E_{obj} from the opaque target object at temperature T_{obj} and the reflected radiation E_{ref} from a remote thermal source at temperature T_{ref}:

$$E_{tot} = \epsilon E_{obj} + \rho E_{ref} \tag{2}$$

The atmosphere between the target object and the thermal camera is usually a cause of perturbation in measurement so that the incident radiation can be attenuated due to atmospheric conditions. According to [27], Eq. (2) can be rewritten considering the atmospheric transmittance τ_{atm} as:

$$E_{tot} = \tau_{atm}(\epsilon E_{obj} + \rho E_{ref}) + (1 - \tau_{atm}) E_{atm} \tag{3}$$

where E_{atm} is the amount of radiation emitted by the atmosphere at an ambient temperature of T_{atm}. In normal atmospheric conditions (no sprays, mists, fog, or precipitations in the atmosphere), the atmospheric constituents that contribute significantly to the attenuation of the radiation are water vapor and carbon dioxide [28].

III. Material

The thermal cameras used in this study are delivered by MOBOTIX. Each installation consists of a Mx-S16B camera module and two Mx-O-SMA-TPR079 thermal sensor modules [29]. The thermal sensor modules consist of an uncooled microbolometer developed by FLIR, a lens, and a housing to mount the sensor modules to the ceiling. The microbolometer is operating in the spectral range from 7.5 to 13.5 μm with noise equivalent temperature difference (NETD) typical of 50 mK (< 79 mK), and is calibrated for temperature events from $-40°$ to 550°C. The lens has a field of view of $45° \times 32°$ with a focal length of 7 mm. The maximum image size is 336×252 pixels with a maximum frame rate of 9 frames per second. Three thermal compensation parameters can be configured for calculating temperature values: object emissivity, atmospheric transmittance, and ambient temperature. The sensors have a flat-field correction mechanism for self-calibration. A shutter with uniform temperature is presented to every detector element to update the sensor correction coefficients, resulting in a more uniform array output. The process takes less than 0.5 seconds and is induced based on elapsed time and the sensor module's temperature.

The black body JQ-D70Z used in our experiments is from Dahua Technology [30]. It emits thermal radiation at a set temperature on a surface of 70 by 70 mm. The following parameters are reported for the black body: resolution of 0.1°C, accuracy of ± 0.2°C, stability of $\pm(0.1$ to $0.2)$°C and emissivity of 0.97 ± 0.01.

For logging actual room temperature values, the MicroLite LITE5032P-RH USB data logger [31] was used. The device has a temperature range of -40 to 80°C, an accuracy of ± 0.3°C, and a resolution of ± 0.01°C.

IV. Experiments and Results

In each delivery room, two sensor modules were mounted to the ceiling: behind the bed (head sensor) and on the side of the bed (side sensor), as illustrated in Fig. 1. Four experiments were carried out to gain a better understanding of the factors influencing temperature measurements in delivery rooms. The temperature of the black body was set to 36°C, similar to the human skin temperature. Object emissivity was set to 0.97 in the sensor settings. Ambient temperature was set to a fixed value corresponding to the room temperature at the beginning of each experiment. At any time sample n, let $T_m(\mathbf{x}, n)$ denote the measured temperature, where $\mathbf{x} = [x\, y]^T$

TABLE I. EXP. 1. INFORMATION RELATED TO THE THERMAL VIDEOS RECORDED.

Room	Sensors	τ_{atm} (head / side)	Video Length (frames)
1	1 & 2	1.00 / 1.00	14858
2	3 & 4	1.00 / 1.00	6271
3	5 & 6	0.81 / 0.82	40902

represents the spatial coordinates in the video frame. Deriving the real object temperature T_{obj} by substituting Eq. (1) into Eq. (3), the measured temperature can be modeled as the sum of T_{obj}, noise $w(\mathbf{x}, n)$ expressed in terms of a moving average $\mathrm{MA}(\mathbf{x}, n)$ and a zero-mean Gaussian noise $\mathcal{N}(0, \sigma^2)$, and a variable bias $b(\mathbf{x}, n)$ that depends on several factors, e.g. position relative to the sensor module, angle of view, lens optics, room temperature, and sensor offset:

$$T_m(\mathbf{x}, n) = T_{obj}(\mathbf{x}, n) + w(\mathbf{x}, n) + b(\mathbf{x}, n) \quad (4)$$

$$w(\mathbf{x}, n) = \mathrm{MA}(\mathbf{x}, n) + \mathcal{N}(0, \sigma^2) \quad (5)$$

A. Experiment 1 - Noise Modeling

Two videos (head and side views) from three different delivery rooms were used in this experiment, giving a total of six videos recorded at 8.33 fps. The details of each video can be seen in Tab. I. For the atmospheric transmittance setting, two configurations were considered:

1) *Default configuration*: In room 1 and 2, a real birth was recorded. The default atmospheric transmittance setting in sensors 1 to 4 was used (set to 1.00). To do the evaluation, a non-motion background region was selected. The results are shown in Tab. II.
2) *Configuration with Black Body*: The black body can be used for configuring the atmospheric transmittance and, thus, compensating for distance to the camera. For head and side sensors in room 3, this parameter was set to 0.81 and 0.82 respectively, based on reference measurements of the black body placed at the position where the newborn baby is expected to be. The black body surface was used as region of interest for evaluation. Results are presented in Tab. III.

To model the noise $w(\mathbf{x}, n)$, a fixed set of pixels was evaluated over time, illustrated with the green squares in Fig. 1. For each video, the pixel set was placed on the same non-motion region of interest seen from both head and side sensor modules to have homogeneous temperature values over time. Let S_x define a subset of corner and center pixel coordinates of an 11 by 11 sized box. Moving windows n_l of length 1 second, 10 seconds, 60 seconds, and the full video (n_1, n_{10}, n_{60}, and n_L, respectively) were used to analyze noise in temperature. For each $\mathbf{x}' \in S_x$, the range and the signal-noise ratio (SNR) were calculated using moving windows of length. Results are presented as the average of the five pixels in S_x.

$$\mathrm{Range}_{\mathbf{x}',n_l} = \max(T_m(\mathbf{x}', n_l)) - \min(T_m(\mathbf{x}', n_l)) \quad (6)$$

$$\mathrm{SNR}_{\mathbf{x}',n_l} = 20 \log \left(\frac{\mu_{\mathbf{x}',n_l}}{\sigma_{\mathbf{x}',n_l}} \right) \quad (7)$$

B. Experiment 2 - Dynamic scene changes

In real births, people involved are continuously moving. The second experiment aimed to analyze the effect of the bias term $b(\mathbf{x}, n)$ when changing the target object's position relative to the sensor module, illustrated with the blue squares in Fig. 1. This experiment was conducted in an empty room, using only one sensor module. The black body was used as target object. The ambient temperature and atmospheric transmittance parameters were set to 23°C and 0.85, respectively. The initial distance between the sensor module and the black body was 3 meters, similar to the distance to the region of interest in the delivery rooms at the hospital. For each video frame, the black body surface was found and measured. Results from placing the black body at different positions are depicted as box plots in Fig. 2. Temperature differences of ±0.3°C were seen when displacing the black body from its initial position.

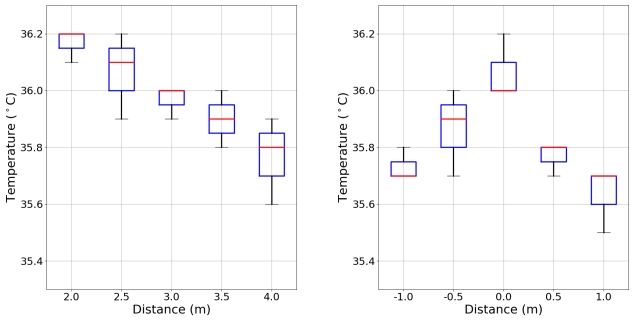

Fig. 2. Exp. 2: The sensor configuration is set with the black body at 36°C, at a distance of 3 meters to the sensor module. Left: the black body is moved from front to back, staying centered in the video frame. Right: the black body is moved from left to right, staying at 3 meters of distance.

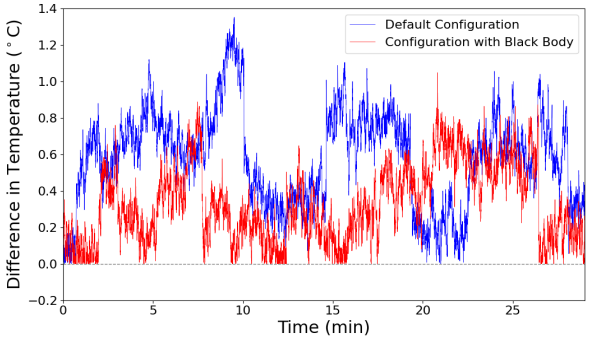

Fig. 3. Exp. 3: Absolute difference in temperature between the measurements taken from the two sensor modules mounted in the same delivery rooms. In blue, the sensors used the default configuration for the atmospheric transmittance. In red, the black body was used to adjust this parameter.

C. Experiment 3 - Offset between Sensor Modules

In each delivery room, each thermal sensor works independently. The goal of this experiment was to compare head and side sensors mounted in the same room when measuring the same region of interest, as illustrated with the yellow squares in Fig. 1. Videos from room 1 and room 3 were used to calculate the absolute difference for each sensor pair. Similar to Exp. 1, pixels in S_x were evaluated. The absolute difference between head and side sensors of the average of the pixels in S_x is represented in Fig. 3.

TABLE II. EXP. 1. NOISE MODELING FOR DEFAULT CONFIGURATION.

	Range (°C)								SNR (dB)			
	Avg (std)				Max				Avg (std)			
Window Size	**Sen 1**	**Sen 2**	**Sen 3**	**Sen 4**	**Sen 1**	**Sen 2**	**Sen 3**	**Sen 4**	**Sen 1**	**Sen 2**	**Sen 3**	**Sen 4**
1 sec	0.06 (0.05)	0.09 (0.06)	0.08 (0.05)	0.07 (0.05)	0.76	0.64	0.76	0.80	136.35 (8.89)	129.2 (13.26)	135.55 (9.42)	136.44 (9.58)
10 sec	0.26 (0.10)	0.29 (0.09)	0.27 (0.08)	0.28 (0.11)	0.80	0.80	0.84	0.84	119.55 (7.52)	115.4 (7.98)	120.18 (5.53)	117.81 (8.15)
60 sec	0.52 (0.15)	0.52 (0.11)	0.47 (0.11)	0.58 (0.19)	0.92	0.92	0.96	1.60	107.27 (7.86)	108.48 (7.34)	112.77 (5.12)	105.88 (7.15)
Full Video	1.50	1.66	0.97	1.29	1.60	2.00	1.12	1.64	86.54	78.72	100.59	90.27

TABLE III. EXP. 1. NOISE MODELING WHEN CONFIGURING WITH BLACK BODY.

	Range (°C)				SNR (dB)	
	Avg (std)		Max		Avg (std)	
Window Size	**Sen 5**	**Sen 6**	**Sen 5**	**Sen 6**	**Sen 5**	**Sen 6**
1	0.09 (0.06)	0.07 (0.07)	1.52	1.36	141.92 (10.05)	143.53 (9.89)
10	0.30 (0.12)	0.29 (0.17)	1.68	1.52	125.08 (6.39)	125.56 (8.09)
60	0.55 (0.20)	0.62 (0.33)	1.68	1.76	117.48 (7.12)	114.62 (11.01)
Full Video	1.66	2.39	1.84	2.44	99.09	88.37

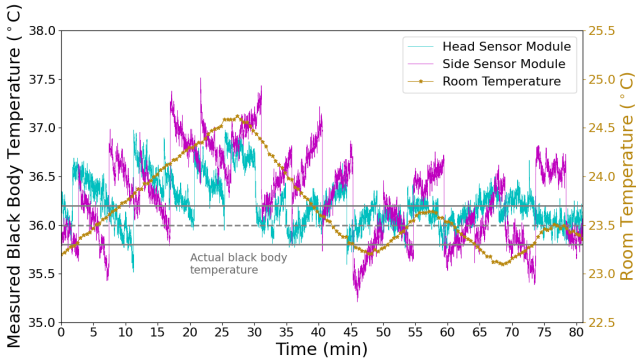

Fig. 4. Exp. 4: Temperature measurements on the black body surface from head and side sensor modules in room 3 along with the room temperature. Black body temperature is expected to be 36 ± 0.2°C.

D. Experiment 4 - Effect of Room Temperature

In room 3, the room temperature was logged every 30 seconds using the MicroLite data logger. This experiment aimed to evaluate the impact of the room temperature on the measurements, illustrated with the red squares in Fig. 1. The black body surface was used as region of interest. The temperature data logger was placed near the black body. A evaluation of room temperature and drifting in temperature values is shown in Fig. 4.

V. DISCUSSION

Exp. 1 aimed to model the noise in the measurements. From Tab. II, a slight variation in the temperature values in concordance with the NETD value provided in the thermal sensor datasheet ($<$ 79 mK) can be noticed when evaluating very short periods of time. The effect of the flat-field correction mechanism can be seen looking at the maximum range for small windows, where abrupt temperature changes occur in short times. Along with this, temperature range increases in terms of mean value, standard deviation, and maximum value with longer windows. This means that there is a more considerable drift in the temperature values when evaluating longer time sequences. Although fluctuations were expected to be reduced by utilizing a black body for configuring the thermal sensor, its use did not improve the sensor's behavior in terms of noise and drifting, as shown in Tab. III. Placing a black body near the target object or the region of interest at all times is usually recommended for providing a reference temperature point in the field of view of the sensor modules. However, for the birth scenario, this option is not physically feasible.

Explaining the variable bias is a complex task. Exp. 2 allowed us to evaluate the changes in temperature values when moving a target object. The effect of other factors can be more challenging to assess. The lens optics may cause variations in the behavior of pixels further away from each other, implying that the lens effect has less impact in the center of the image than in the corners when considering the same distance to the sensor module. The sensor offset is another factor to take into consideration when referring to the bias term. Together with this, controlling the flat-field correction mechanism is not easy, and it needs to be synchronized between sensor modules to make a proper measurement comparison. Due to all this, as shown in Exp. 3, a disparity of up to 1.5°C exists when comparing the measurements between both sensors.

At the same time, the transmission coefficient directly leverages the ambient temperature value, as shown in Eq. (3), so the lower the atmospheric transmittance is, the greater influence the ambient temperature will have on the overall measurement. This means that room temperature has a significant impact when measuring, generating a drifting in the temperature values. As delivery rooms are connected to the same heating system, the behavior in Fig. 4 is expected to happen in all delivery rooms. This is challenging for the birth scenario, as considerable and non-uniformly distributed variations in room temperature can exist during labor.

VI. CONCLUSION

In this paper, we have investigated the challenges of using a dual thermal sensor setup for detecting the exact time of birth in delivery room environments, where accurate temperature measurements would be desirable. We showed that the variation in the thermal sensors consists of a combination of short-time random noise, drift, self-calibration steps, and room temperature. This all imposes challenges preventing the temperature measurements from being used directly for the time of birth detection. The performance of other uncooled commercial thermal sensors is expected to be similar to that shown in our experiments, since most of these sensors are based on FLIR technology. Future work will concentrate on testing different strategies to compensate for drifting in temperature values, and make it possible to utilize thermal imaging to develop an accurate AI-based time of birth detector.

REFERENCES

[1] R. Bhan, R. Saxena, C. Jalwani, and S. Lomash, "Uncooled infrared microbolometer arrays and their characterisation techniques," *Defence Science Journal*, vol. 59, no. 6, p. 580, 2009.

[2] L. Yu, Y. Guo, H. Zhu, M. Luo, P. Han, and X. Ji, "Low-cost microbolometer type infrared detectors," *Micromachines*, vol. 11, no. 9, p. 800, 2020.

[3] M. Ball and H. Pinkerton, "Factors affecting the accuracy of thermal imaging cameras in volcanology," *Journal of Geophysical Research: Solid Earth*, vol. 111, no. B11, 2006.

[4] R. Usamentiaga, P. Venegas, J. Guerediaga, L. Vega, J. Molleda, and F. G. Bulnes, "Infrared thermography for temperature measurement and non-destructive testing," *Sensors*, vol. 14, no. 7, pp. 12 305–12 348, 2014.

[5] B. Wang, S. Zhong, T.-L. Lee, K. S. Fancey, and J. Mi, "Non-destructive testing and evaluation of composite materials/structures: A state-of-the-art review," *Advances in mechanical engineering*, vol. 12, no. 4, p. 1687814020913761, 2020.

[6] M. S. Jadin and K. H. Ghazali, "Gas leakage detection using thermal imaging technique," in *2014 UKSim-AMSS 16th International Conference on Computer Modelling and Simulation*, 2014, pp. 302–306.

[7] V. Sagan, M. Maimaitijiang, P. Sidike, K. Eblimit, K. T. Peterson, S. Hartling, F. Esposito, K. Khanal, M. Newcomb, D. Pauli *et al.*, "Uav-based high resolution thermal imaging for vegetation monitoring, and plant phenotyping using ici 8640 p, flir vue pro r 640, and thermomap cameras," *Remote Sensing*, vol. 11, no. 3, p. 330, 2019.

[8] M. Krišto, M. Ivasic-Kos, and M. Pobar, "Thermal object detection in difficult weather conditions using yolo," *IEEE Access*, vol. 8, pp. 125 459–125 476, 2020.

[9] A. Akula, A. K. Shah, and R. Ghosh, "Deep learning approach for human action recognition in infrared images," *Cognitive Systems Research*, vol. 50, pp. 146–154, 2018.

[10] Q. Ha, K. Watanabe, T. Karasawa, Y. Ushiku, and T. Harada, "Mfnet: Towards real-time semantic segmentation for autonomous vehicles with multi-spectral scenes," in *2017 IEEE/RSJ International Conference on Intelligent Robots and Systems (IROS)*, 2017, pp. 5108–5115.

[11] E. Ring and K. Ammer, "Infrared thermal imaging in medicine," *Physiological measurement*, vol. 33, no. 3, p. R33, 2012.

[12] S. J. Mambou, P. Maresova, O. Krejcar, A. Selamat, and K. Kuca, "Breast cancer detection using infrared thermal imaging and a deep learning model," *Sensors*, vol. 18, no. 9, p. 2799, 2018.

[13] C. Herman and M. P. Cetingul, "Quantitative visualization and detection of skin cancer using dynamic thermal imaging," *Journal of visualized experiments: JoVE*, no. 51, 2011.

[14] S. Kumar, A. Iftekhar, M. Goebel, T. Bullock, M. H. MacLean, M. B. Miller, T. Santander, B. Giesbrecht, S. T. Grafton, and B. Manjunath, "Stressnet: detecting stress in thermal videos," in *Proceedings of the IEEE/CVF Winter Conference on Applications of Computer Vision*, 2021, pp. 999–1009.

[15] S. Shaikh, N. Akhter, and R. Manza, "Current trends in the application of thermal imaging in medical condition analysis," *Int. J. Innov. Technol. Explor. Eng*, vol. 8, no. 8, pp. 2708–2712, 2019.

[16] A. Barnawi, P. Chhikara, R. Tekchandani, N. Kumar, and B. Alzahrani, "Artificial intelligence-enabled internet of things-based system for covid-19 screening using aerial thermal imaging," *Future Generation Computer Systems*, vol. 124, pp. 119–132, 2021.

[17] B. Peddinti, A. Shaikh, B. K.R., and N. K. K.C., "Framework for real-time detection and identification of possible patients of covid-19 at public places," *Biomedical Signal Processing and Control*, vol. 68, p. 102605, 2021. [Online]. Available: https://www.sciencedirect.com/science/article/pii/S1746809421002020

[18] R. Kitchin, "Civil liberties or public health, or civil liberties and public health? using surveillance technologies to tackle the spread of covid-19," *Space and Polity*, vol. 24, no. 3, pp. 362–381, 2020.

[19] M. Tkáčová, R. Hudák, P. Foffová, and J. Živčák, "An importance of camera–subject distance and angle in musculoskeletal applications of medical thermography," *Acta Electrotechnica et Informatica*, vol. 10, no. 2, pp. 57–60, 2010.

[20] I. Pušnik and G. Geršak, "Evaluation of the size-of-source effect in thermal imaging cameras," *Sensors*, vol. 21, no. 2, p. 607, 2021.

[21] P. R. Muniz, S. P. Cani, and R. d. S. Magalhaes, "Influence of field of view of thermal imagers and angle of view on temperature measurements by infrared thermovision," *IEEE Sensors Journal*, vol. 14, no. 3, pp. 729–733, 2013.

[22] M. Litwa, "Influence of angle of view on temperature measurements using thermovision camera," *IEEE Sensors Journal*, vol. 10, no. 10, pp. 1552–1554, 2010.

[23] *Infrared Radiation*. John Wiley & Sons, Ltd, 2007. [Online]. Available: https://onlinelibrary.wiley.com/doi/abs/10.1002/0471743984.vse4181.pub2

[24] G. Gaussorgues and S. Chomet, *Infrared thermography*. Springer Science & Business Media, 1993, vol. 5.

[25] G. ElMasry, R. ElGamal, N. Mandour, P. Gou, S. Al-Rejaie, E. Belin, and D. Rousseau, "Emerging thermal imaging techniques for seed quality evaluation: Principles and applications," *Food Research International*, vol. 131, p. 109025, 2020.

[26] V. Bernard, E. Staffa, V. Mornstein, and A. Bourek, "Infrared camera assessment of skin surface temperature–effect of emissivity," *Physica Medica*, vol. 29, no. 6, pp. 583–591, 2013.

[27] M. J. Harrap, N. Hempel de Ibarra, H. M. Whitney, and S. A. Rands, "Reporting of thermography parameters in biology: a systematic review of thermal imaging literature," *Royal Society open science*, vol. 5, no. 12, p. 181281, 2018.

[28] W. Minkina and D. Klecha, "Atmospheric transmission coefficient modelling in the infrared for thermovision measurements," *Journal of Sensors and Sensor Systems*, vol. 5, no. 1, pp. 17–23, 2016.

[29] *Technical Specifications MOBOTIX S16B DualFlex*, MOBOTIX AG, 12 2021. [Online]. Available: https://www.mobotix.com/sites/default/files/2019-03/Mx_TS_S16B_en_20190314.pdf

[30] *JQ-D70Z Thermometric Blackbody*, Dahua Technologyr, 2020, rev. 001.001. [Online]. Available: https://www.dahuasecurity.com/asset/upload/uploads/soft/20200417/JQ-D70Z_Datasheet_New_20200321.pdf

[31] *MicroLite. Portable cable free USB loggers.*, FOURTEC, 2021, rev 5.15. [Online]. Available: https://fourtec.com/wp-content/Downloads/MicroLite%20Brochure%202021.pdf